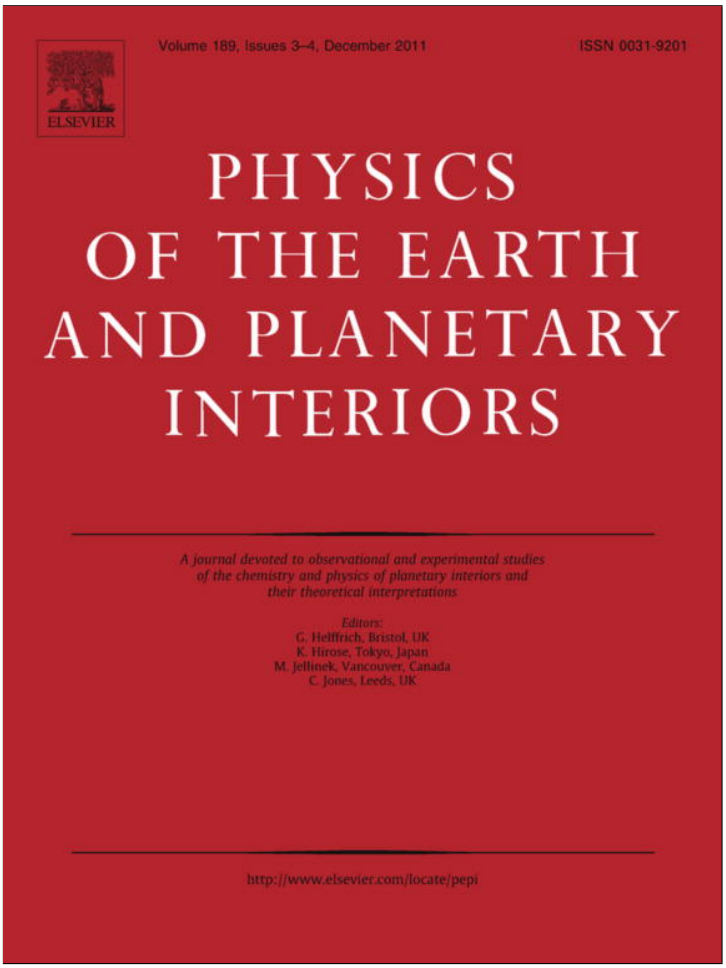

Physics of the Earth and Planetary Interiors 189 (2011) 176–184

Contents lists available at SciVerse ScienceDirect

Physics of the Earth and Planetary Interiors

journal homepage: www.elsevier.com/locate/pepi

Seismic velocity structures and detailed features of the D″ discontinuity near the core-mantle boundary beneath eastern Eurasia

Yumei He [a,b,*], Lianxing Wen [b,c]

[a] Key Laboratory of the Earth's Deep Interior, Institute of Geology and Geophysics, Chinese Academy of Sciences, Beijing 100029, PR China
[b] Department of Geosciences, State University of New York at Stony Brook, Stony Brook, NY 11790, USA
[c] School of Earth and Space Sciences, University of Science and Technology of China, Hefei, Anhui 230026, PR China

ARTICLE INFO

Article history:
Received 9 February 2011
Received in revised form 23 August 2011
Accepted 6 September 2011
Available online 8 September 2011

Keywords:
Seismic velocity structure
Core-mantle boundary
D″ discontinuity
Eastern Eurasia

ABSTRACT

Shear and compressional velocity structures and features of the D″ discontinuity near the core-mantle boundary (CMB) beneath eastern Eurasia are studied based on forward waveform modeling and differential-travel-time analysis of ScSH-SH, sScS-sS, PcP-P and pPcP-pP phases. High-quality differential-travel-time analysis reveals two high-velocity patches spanning a width of 3000 km and separated by a 300-km wide normal velocity gap. The maximum shear and compressional velocity perturbations reach 3.8% and 2.7%, respectively. Seismic data indicate that the D″ discontinuity emerges in the high velocity patches and disappears in the normal-velocity gap. Furthermore, the features of the D″ discontinuity, although constrained by rather sparse seismic data, vary from diffusive discontinuities in the eastern patch to sharp discontinuities in the western patch. The D″ discontinuities occur at about 270 km above the CMB in the eastern patch with a shear velocity jump of 3.0–5.0% and a transitional depth of at least 100 km, and at 250 km above the CMB in the western patch with an abrupt shear velocity jump of 5.0%. A diffusive P wave discontinuity is also observed in the eastern patch with the similar features of the S wave discontinuity. The inferred features of the D″ discontinuity can be explained by the post-perovskite transformation in the lower mantle. The observations that the D″ discontinuities occur only in the high-velocity patches may be due to the effect of the positive Clapeyron slope of the post-perovskite transition, and the varying transitional depths of the D″ discontinuity in the high-velocity regions may be caused by the compositional effects on the post-perovskite transition in the presence of strong variations of composition within the high-velocity anomalies. The high-velocity patches geographically correlate with the subduction of the Pacific and Indian plates in the past 30–60 Ma, and the normal-velocity gap falls into the subduction gap between the Pacific and Indian plates. These geographical correlations raise the possibility that the existence of the D″ discontinuity is intimately related to the presence of the past subduction material at the CMB, and varying features of the discontinuity further suggest existence of strong variations of composition within the subduction materials at the CMB.

1. Introduction

Tomographic images have shown a belt of high velocity anomalies in the D″ region (defined as the lowermost 200–300 km of the mantle) beneath the circum-Pacific (e.g., Van der Hilst and Kárason, 1999; Ritsema and van Heijst, 2000; Grand, 2002; Zhao, 2004; Li et al., 2008). Mainly in these high velocity regions, seismic studies have also revealed intermittent existence of a D″ discontinuity at 200–300 km above the core-mantle boundary (CMB) (Lay and Helmberger, 1983). The seismic observations of the D″ discontinuity remain puzzling. The discontinuity emerges and disappears over a small distance range (Wysession et al., 1998; Lay et al., 2004); its characteristics varies from a sharp discontinuity to a diffusive one with a transitional depth of a few tens of kilometers (Lay, 2008); and while an S wave discontinuity is usually observed for the D″ layer, it correlates with a large positive P wave discontinuity in some regions (Weber and Davis, 1990; Thomas et al., 2002, 2004), and no or a small negative P wave discontinuity in other regions (Weber, 1993; Ding and Helmberger, 1997; Kito et al., 2007; Hutko et al., 2008; Chaloner et al., 2009). In the interpretation of the D″ discontinuity, the post-perovskite transition has been proposed as a possible candidate (Murakami et al., 2004; Oganov and Ono, 2004; Wookey et al., 2005; Hirose, 2006; Shim, 2008; Catalli et al., 2009). However, it remains unclear how the phase transition is related to the intermittent presence and detailed features of the D″ discontinuity.

In this study, we determine both seismic velocity structures and features of the D″ discontinuity near the CMB beneath eastern

* Corresponding author at: Key Laboratory of the Earth's Deep Interior, Institute of Geology and Geophysics, Chinese Academy of Sciences, Beijing 100029, PR China. Tel.: +86 10 82998416.
E-mail address: ymhe@mail.igcas.ac.cn (Y. He).

0031-9201/$ - see front matter © 2011 Elsevier B.V. All rights reserved.
doi:10.1016/j.pepi.2011.09.002

Eurasia (10–60°N and 75–130°E) using ScSH-SH, sScS-sS, PcP-P and pPcP-pP differential travel times and forward waveform modeling. The study region is characterized by fast velocities in global tomography models and coincides with the reconstructed position of ancient Indian and Pacific subduction. Through determination of high-resolution small-scale velocity anomalies and detailed features of the D″ discontinuity, we explore possible connections among the observed features of the D″ discontinuity, velocity anomalies in the lowermost mantle and the past subduction, combining the results of the post-perovskite phase change and the reconstruction of past subduction histories. We show seismic data in Section 2, infer high-resolution compressional and shear velocity structures in the lowermost mantle and study the detailed D″ discontinuity features in several cross-sections in Section 3, and discuss the relationships between the inferred features of the D″ discontinuity, seismic velocity anomalies, post-perovskite transformation and past subduction history in Section 4.

2. Seismic data

We focus our study area on a region near the CMB between 10–60°N and 75–130°E. We use ScSH-SH, sScS-sS, PcP-P and pPcP-pP differential travel time measurements to infer seismic shear and compressional velocity structures near the CMB and employ waveform modeling to constrain the detailed features of the D″ discontinuity in the region. The use of differential travel times minimizes the uncertainties of source mislocation and the effects of seismic heterogeneities in the upper mantle.

We collect broadband tangential displacements recorded at a distance range between 45° and 85° for ScSH-SH and sScS-sS travel time analysis. We check all seismic data sampling the study region from 1994 to 2011 for earthquakes with a magnitude >5.8. We finally select 44 earthquakes (Table 1) with high signal-to-noise ratios and obtain a total of 674 ScS-S and 53 sScS-sS travel time residuals. The seismic data provide dense coverage in our study area (Fig. 1a). The events and stations are mainly located in the east, west and south of Eurasia. Part of the ScS-S and all sScS-sS differential travel times are selected from the seismic data recorded in the F-net in Japan, the China National Seismic Network (CNSN), the Malaysian National Seismic Network (MY) and several permanent stations in the Global Seismographic Network (GSN), for earthquakes occurring in western Asia. We also use the seismic data recorded in several PASSCAL arrays and four regional networks: CNSN, MY, Kyrgyz Seismic Telemetry Network (KNET) and Kazakhstan Network (KZNET), as well as several permanent stations in the GSN and GEOFON, for earthquakes occurring in the western Pacific subduction zone.

We collect broadband vertical displacements recorded at a distance range between 45° and 75° for PcP-P and pPcP-pP differential travel time analysis. We select 19 earthquakes occurring from 1994 to 2010, and obtain a total of 226 PcP-P and 20 pPcP-pP travel time residuals (Table 2). Three events occurred in western Asia and are recorded at the GSN, the CNSN and the F-net, the others are selected from the seismic data recorded in KNET, KZNET, and several permanent stations in the CNSN and GSN, for earthquakes mainly occurring in the western Pacific subduction zone (Fig. 1b).

We use waveforms recorded in northwest Asia for four events occurring in southern Sumatra, Java sea, Bali sea and Banda sea to constrain the detailed features of the D″ discontinuity in the region. For each event, we select observations within a small azimuthal range of 6° to minimize the effects of lateral variation of seismic structure. The tangential and vertical waveforms are deconvolved with their instrumental responses and bandpass-filtered from 0.008 to 1 Hz.

3. Velocity structures and features of the D″ discontinuity in the region

3.1. Shear and compressional velocity structures based on ScS-S, sScS-sS, PcP-P and pPcP-pP differential travel times

We infer shear and compressional velocity structures in the lowermost 300 km of the mantle based on the following procedures: we first measure ScS-S, sScS-sS, PcP-P and pPcP-pP differential travel time residuals from the tangential and vertical components of seismograms; we then remove the contributions due to seismic heterogeneities 300 km above the CMB from the observed differential travel time residuals based on seismic tomographic models; and we derive seismic velocity anomalies in the lowermost 300 km of the mantle from the corrected ScS-S, sScS-sS, PcP-P and pPcP-pP differential travel time residuals.

We measure ScS-S differential travel times by the difference of peak-to-peak times of the two phases on the transverse components of seismograms. By hand-picking the peaks of the S and ScS phases in various frequency bands and comparing the results, we estimate the uncertainty in the measurements of the differential travel times to be 1.0 s. We test many tomographic models in the corrections for the contributions of the seismic heterogeneities 300 km above the CMB (Grand, personal communication; Gu and Dziewonski, 1999; Masters et al., 2000; Mégnin and Romanowicz, 2000; Ritsema and van Heijst, 2000; Ritsema et al., 2010). We select the model for the corrections based on the following criterion. For each model, we calculate the correlations between two groups of the corrected residuals, S travel time residuals vs ScS-S differential travel time residuals, and ScS travel time residuals vs ScS-S differential travel time residuals (He et al., 2006). If the corrected ScS-S travel time residuals are mostly contributed by the seismic heterogeneities in the lowermost mantle, there would be no correlation between the corrected S travel time residuals and ScS-S differential travel time residuals, and a strong correlation between the corrected ScS travel time residuals and ScS-S differential travel time residuals. Based on this criterion, we choose model S20RTS (Ritsema and van Heijst, 2000) for corrections as that model produces the best correlation between the corrected ScS travel time residuals and ScS-S differential travel time residuals, and removes the anti-correlation between the observed S travel time residuals and ScS-S differential travel time residuals most. We also adopt the same criterion for correcting the sScS-sS differential travel times. The corrected ScS-S and sScS-sS differential travel times show large and strongly laterally varying residuals (Fig. 2a). These residuals can be explained by a combination of varying thickness of a layer with a higher-than-average velocity perturbation and lateral varying velocity perturbations in the lowermost mantle. Without further constraints on the velocity structure, we present a simple model, attributing the corrected ScS-S and sScS-sS differential travel times to lateral velocity variations in the lowermost 300 km of the mantle. The inferred shear velocity perturbations exhibit two high-velocity patches separated by a normal velocity gap (Fig. 2b). The highest shear velocity perturbation reaches 3.8% around (39°N, 101°E) (Fig. 2b). High velocities are prevalent throughout the whole eastern part of the study area except in the southeast corner. In the west of the study area, high velocity anomaly exhibits a reversed "L-shaped" form changing from an east–west orientation between 35°N and 48°N to a north–south orientation around 90°E. Normal or low velocities surround the reversed "L-shaped" high velocity anomaly. The shape of the high velocity anomalies coincides remarkably well with the geometry of the past subduction in the past 30–60 Ma (updated from Wen and Anderson, 1995 by adding the past subduction along the eastern Tibet and projecting the trench locations with realistic subduction angles in the upper mantle). The eastern and western

Table 1
Events for ScSH-SH and sScS-sS travel time analysis.

Number[a]	Origin time	Latitude (°N)	Longitude (°E)	Depth (km)
	1994.09.28.16.39.52	−5.75	110.28	653
	1995.10.01.17.06.03	29.31	138.95	427
	1996.03.16.22.04.06	29.12	139.12	478
	1996.06.26.03.22.03	27.82	139.85	479
	1996.07.06.21.36.28	21.97	142.83	241
	1996.07.20.09.14.04	13.87	120.48	119
	1996.08.10.18.12.17	38.91	140.53	10
	[b]1997.02.27.21.08.02	29.98	68.21	33
1	1997.07.11.09.55.12	−5.70	110.80	574
	1997.10.06.12.30.05	9.79	125.78	106
	1999.01.12.02.32.25	26.74	140.17	441
	1999.03.28.19.05.13	30.51	79.40	15
	1999.08.14.00.16.52	−5.89	104.71	101
	1999.11.11.18.05.43	1.28	100.32	211
	2000.06.09.23.31.45	30.49	137.73	485
3	2000.08.07.14.33.55	−7.02	123.36	649
	[b]2001.01.26.03.16.40	23.42	70.23	16
2	2001.02.16.05.59.09	−7.16	117.49	521
	2002.06.16.18.31.10	−2.34	102.56	232
	2002.06.28.17.19.30	43.75	130.67	566
	2003.05.26.23.13.29	6.90	123.85	580
	2003.07.01.05.52.25	4.69	122.67	605
	2003.09.01.23.16.35	38.57	75.27	10
	2003.10.04.14.49.02	−6.96	125.43	533
	2003.11.12.08.26.43	33.17	137.07	384
	2004.04.05.21.24.04	36.52	70.84	184
	2004.05.28.12.38.46	36.25	51.62	17
	2004.07.25.14.35.19	−2.43	103.98	582
	2004.10.15.04.08.50	24.48	122.74	102
	2005.02.05.12.23.18	5.29	123.34	525
	2005.02.22.02.25.22	30.74	56.83	14
	2006.04.25.18.26.17	1.99	96.99	21
4	2006.11.14.14.21.02	−6.42	127.98	352
	2007.09.28.13.38.57	22.01	142.67	260
	2008.01.22.17.14.58	1.01	97.44	20
	2008.03.29.17.30.50	2.86	95.30	20
	2008.10.28.23.09.58	30.64	67.35	15
	2009.06.05.03.30.33	41.82	143.45	29
	2009.07.13.10.52.20	−9.13	119.32	67
	2009.08.16.07.38.22	−1.48	99.49	20
	2009.09.07.22.41.37	42.66	43.44	15
	2009.10.15.12.11.16	−3.06	139.54	105
	2009.12.10.02.30.52	53.42	152.76	656
	2009.12.24.00.23.33	42.23	134.70	411

[a] Earthquakes used to constrain the velocity structures and features of D″ discontinuity. Events are represented by corresponding numbers in Figs. 3 and 4.
[b] sScS-sS differential travel time residuals are used.

high-velocity patches overlay with the locations of the subducted Pacific Plate and Indian Plate in the past 30–60 Ma, respectively, while the normal velocity gap falls into the subduction gap between the Indian Plate and the Pacific Plate in the past 30–60 Ma (Fig. 2b).

For P wave study, we remove the contributions due to the seismic heterogeneities 300 km above the CMB from the observed PcP-P differential travel time residuals based on the predictions of three tomographic models (van der Hilst and Kárason, 1999; Zhao, 2004; Obayashi et al., 2006). After comparing the correlations between two groups of the corrected values, P travel time residuals vs PcP-P travel time residuals, and PcP travel time residuals vs PcP-P travel time residuals, we finally choose van der Hilst's model for corrections. Only the data with a strong correlation between the corrected PcP travel time residuals and PcP-P differential travel time residuals and no correlation between the corrected P travel time residuals and PcP-P differential travel time residuals are selected. Same procedures are also applied to the corrections for pPcP-pP differential travel times. We infer compressional velocity anomalies from the corrected PcP-P and pPcP-pP travel time residuals following the similar procedures of inferring the shear velocity anomalies from the corrected differential ScS-S and sScS-sS travel time residuals. The corrected PcP-P and pPcP-pP differential travel times show negative travel-time residuals (corresponding to high velocities) beneath eastern China (Fig. 2c). The inferred compressional velocity perturbations show several higher-than-average velocity patches surrounded by normal or low velocity regions (Fig. 2d). The dominant feature is an approximate 1000 × 1500 km high-velocity area in the east, with the largest compressional velocity perturbation reaching 2.7% at (38°N, 112°E). The geometry of the *P* velocity anomaly also matches the geometry of the past Pacific subduction in the region (Fig. 2d).

3.2. Features of the D″ discontinuity from waveform modeling

To study the detailed features of the D″ discontinuity, we perform waveform modeling of shear and compressional seismic data recorded in several stations in eastern Eurasia (WMQ, MKAR, KURK, VOS, BRVK, CHK, ZRNK, and ARU) for 4 events occurring in southern Sumatra, Java sea, Bali sea and Banda sea. All 4 events exhibit simple source time functions and high signal-to-noise ratios. Tangential displacements recorded at ARU are corrected for the effect of the upper mantle anisotropy based on the published results (Silver, 1996). Events 1997/07/11, 2001/02/16, 2000/08/07 and

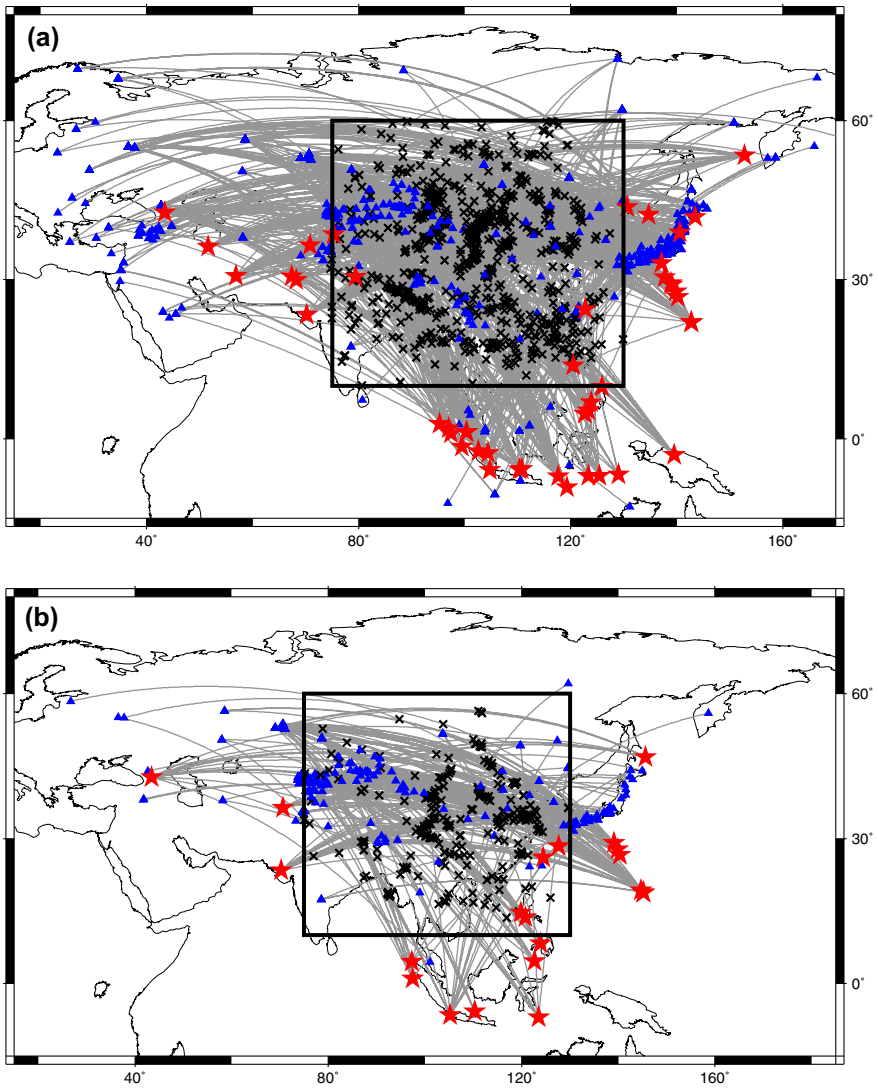

Fig. 1. (a) The region for ScS-S and sScS-sS differential travel time residual study, along with ScS and sScS reflected points at the CMB (crosses), earthquakes (stars), seismic stations (triangles) and great-circle paths (gray lines) of seismic wave propagation. The rectangle box indicates a region where detailed shear velocity results are presented in Fig. 2a and b. (b) Same as (a), except for PcP-P and pPcP-pP differential travel time residual study, along with PcP and pPcP reflected points at the CMB (crosses). The rectangle box indicates a region where detailed P-velocity results are shown in Fig. 2.

Table 2
Events for PcP-P and pPcP-pP travel time analysis.

Origin time	Latitude (°N)	Longitude (°E)	Depth (km)
1994.09.28.16.39.52	−5.75	110.28	653
1995.08.23.07.06.02	18.86	145.22	595
1995.08.24.01.55.34	18.93	145.19	594
1996.06.26.03.22.03	27.82	139.85	479
1998.05.23.17.44.47	8.29	123.86	629
1998.10.03.11.15.42	28.40	127.66	219
1999.01.12.02.32.25	26.74	140.17	441
1999.07.21.13.46.29	4.56	97.26	166
2000.01.28.16.39.24	26.08	124.50	194
2000.07.10.09.58.19	46.83	145.59	361
2000.08.07.14.33.55	−7.02	123.36	649
2000.10.21.22.30.32	13.74	120.81	153
2001.01.26.03.16.40[a]	23.42	70.23	16
2003.07.01.05.52.25	4.69	122.67	605
2004.03.12.22.45.19	36.38	70.60	215
2008.01.22.17.14.58	1.01	97.44	20
2009.09.07.22.41.37	42.66	43.44	15
2009.10.16.09.52.51	−6.53	105.22	38
2010.03.08.09.47.11	19.33	144.71	456

[a] pPcP-pP differential travel time residuals are used.

2006/11/14 (events 1–4 in Fig. 3) sample the study area from west to east. The seismic data for these events sample an area over a distance of about 1000 km, spanning two higher-than-average velocity patches and the gap between them (Fig. 3). The sampling coverage of these events provides a good opportunity to study the relationship between the D″ features and velocity perturbations in the lowermost mantle (Fig. 3).

The SH waves of event 2001/02/16 sample the gap between the two high-velocity patches (event 2 in Fig. 3). Although clear ScS phases are observed suggesting favorable radiation pattern of the event for a potential Scd phase, no secondary phase is observed between S and ScS phases at epicentral distances between 72° and 73°. The non-existence of a secondary phase precludes existence of a significant discontinuity near the CMB. Synthetic tests indicate that a D″ discontinuity with a velocity jump larger than 1% would generate too large an Scd phase to match the data. In fact, the seismic data can be well explained by a model with a linear shear velocity increase no greater than 1% around 200 km above the CMB (Fig. 4(4.2a–c)).

For event 2000/08/07 sampling the eastern high-velocity patch, its tangential components of seismograms show a clear phase be-

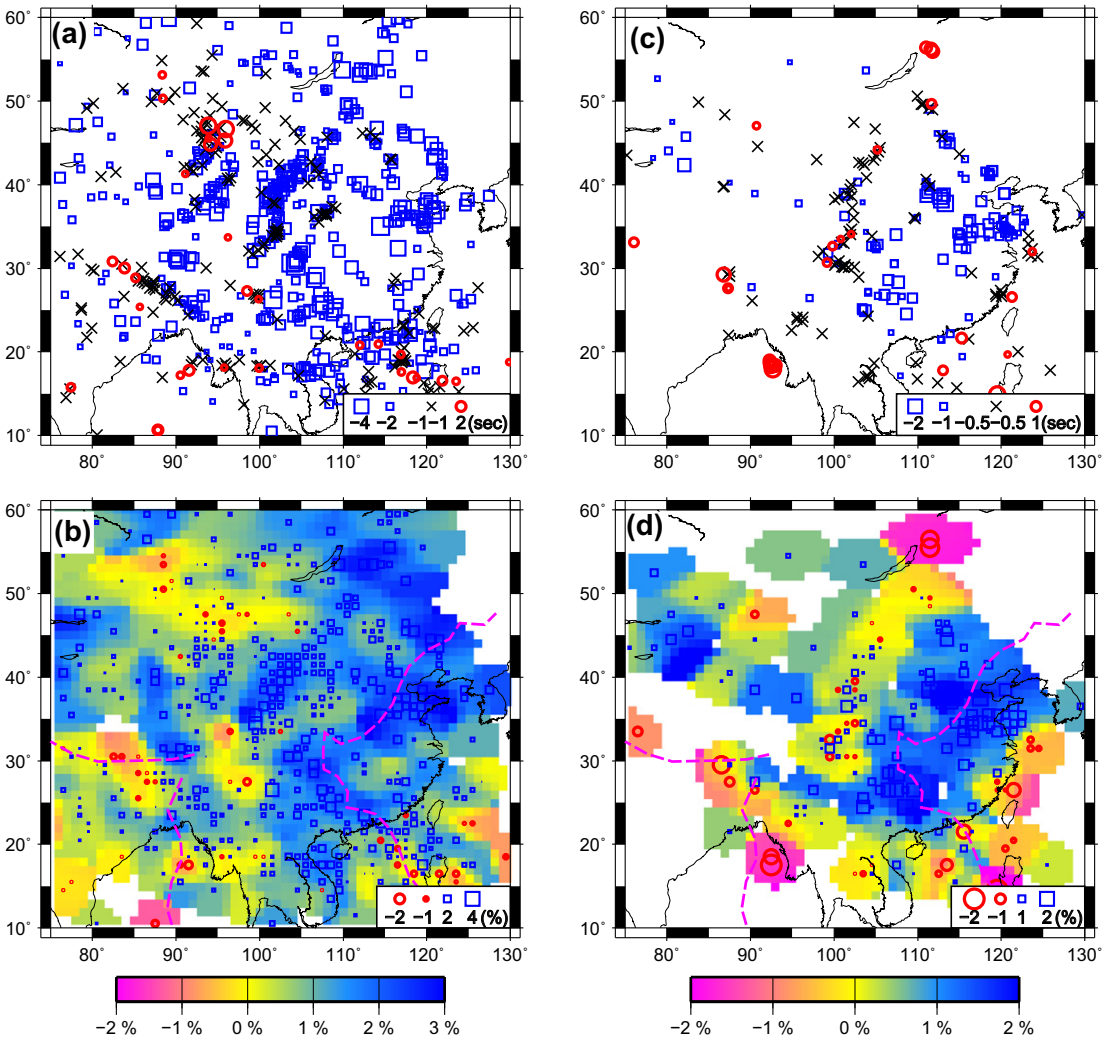

Fig. 2. (a) ScS-S and sScS-sS differential time residuals with respect to the travel time difference predicted from the preliminary reference Earth model (PREM) (Dziewonski and Anderson, 1981) plotted at the ScS reflected points at the CMB. The residuals are corrected for the effects of the mantle heterogeneities 300 km above the CMB, using the S20RTS shear velocity model (Ritsema and van Heijst, 2000). Blue squares, black crosses and red circles represent the residuals smaller than −1 s, from −1 to 1 s, and larger than 1 s, respectively. The sizes of the squares and circles are proportional to the magnitudes of the travel time residuals. (b) Averaged shear velocity perturbations in the bottom 300 km of the mantle inferred from the corrected travel time residuals in (a). For better illustration, the shear velocity perturbations are simply averaged over 1° × 1° grids. Blue squares and red circles represent the velocity increase and reduction, respectively. The shear velocity perturbations are averaged over 1° × 1° grids with a Gaussian cap with a radius of 3° and are shown as background. The distributions of subducted slabs during the past 30–60 Ma (updated from Wen and Anderson, 1995) are also shown by purple dashed lines. (c) same as (a), except for PcP-P and pPcP-pP differential time residuals corrected using a compressional velocity model by Van der Hilst and Kárason (1999). (d) Averaged compressional velocity perturbations in the bottom 300 km of the mantle inferred from the corrected travel time residuals in (c). Symbols, background and purple dashed lines are as similar as those in (b). (For interpretation of the references to color in this figure legend, the reader is referred to the web version of this article.)

tween S and ScS phases at the distance range of 74° and 76° which exhibits large amplitudes and same polarities as S and ScS phases (Fig. 4(4.3a)). That phase is not due to a complex earthquake source, as the recordings at other GSN stations show simple waveforms. It is also not caused by the seismic structures beneath the stations, because the records in these stations for events at closer distances but within a similar azimuth do not show the similar features. It is also unlikely caused by complex seismic structure in the subduction zone, since similar features are observed for events with various focal depths from 180 to 649 km. Besides, the phase between S and ScS exhibits a clear move-out with epicentral distance that is consistent with refraction from a deep discontinuity. We conclude that the most plausible explanation of the observed energy between S and ScS phases is an Scd phase caused by a D″ discontinuity.

The amplitudes and travel times of the Scd phases are sensitive to the detailed features of the D″ discontinuity, including its sharpness, velocity contrast across the discontinuity, and velocity gradients above and below the discontinuity. Event 2000/08/07 provides a good opportunity to investigate the sharpness of the discontinuity. The Scd phases have large amplitudes around 75° and become indiscernible at 69° (Fig. 4(4.3a)). The rapid increase of Scd amplitudes from 69° to 75° cannot be explained by a sharp D″ discontinuity, as a sharp discontinuity that is able to produce the large amplitude of Scd phase at 75° would also generate a strong Scd phase at the small distance of 69° (Fig. 5a and c). Synthetic tests by the hybrid method (Wen, 2002) also indicate that the rapid change of the Scd phases from 69° to 75° can unlikely be produced with two-dimensional (2D) structures. Between these epicentral distances, the separation of the Scd sampling paths in the D″ region is about 170 km. We have performed synthetics calculations for a series of 2D models and are unable to find a suitable model that would produce such rapid change of Scd amplitudes from 69° to 75°. A 2D model that makes Scd phase weak at 69° also produces a weak Scd phase at 75°. The observed rapid change of the Scd amplitudes from 69° to 75° is consistent with a diffusive

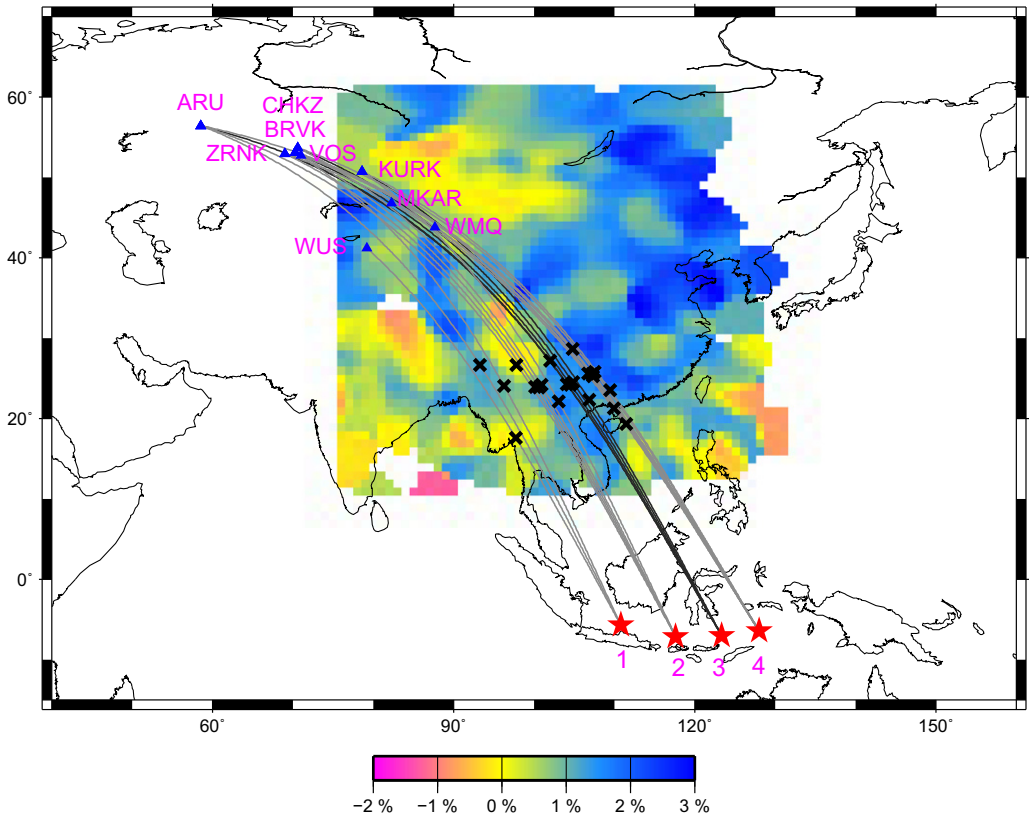

Fig. 3. (a) ScS reflected points (crosses) at the CMB, along with earthquakes (stars), seismic stations (triangles), and great-circle paths (gray lines), for four events (Table 1) whose waveforms are used to constrain the detailed features of the D″ discontinuity inside the high velocity area. Event 3 is studied with both P and SH data and its great-circle paths are plotted with heavy gray lines. Background is the same averaged shear velocity perturbations in the bottom 300 km of the mantle after Gaussian smoothing shown in Fig. 2.

D″ discontinuity with a finite depth transition. The seismic data can be well explained by a discontinuity with a shear velocity jump of 5.0% distributed from 2621 to 2741 km depths, a negative shear velocity gradient above the discontinuity from 0% at 2451 km depth to −1.5% at 2621 km and a negative velocity gradient below the discontinuity to 0% at the CMB (Fig. 4(4.3b and c)). This model is similar to the SYLO model (Young and Lay, 1990), except that this model has a diffusive D″ discontinuity between 2621 and 2741 km depths. The observed rapid reduction of Scd amplitudes from 75° to 69° places a lower bound on the transitional depth of the diffusive discontinuity. For a model with a transitional depth smaller than 120 km, when it explains the large Scd phase at 75°, it would also generate too large an Scd phase at 69° to fit the data. Because there are no other observations available between 69° and 75°, the maximum transitional depth of the diffusive discontinuity cannot be resolved.

The vertical displacements of event 2000/08/07 exhibit similar characteristics as the tangential displacements. They show a strong and clear phase between P and PcP between 74° and 76°, but no discernable phase at 69°. For the same reasons stated for explaining the Scd amplitudes, these characteristics cannot be modeled by a sharp P-wave discontinuity (Fig. 5d). The P wave observations can be explained by a diffusive *P* velocity discontinuity with a velocity jump of 2.8% and a transitional depth of 100 km, a *P* velocity reduction of −0.8% above the discontinuity and a negative velocity gradient below the discontinuity (Fig. 5e and f).

Waveforms of event 2006/11/14 show similar features as those of event 2000/08/07. The Scd phases have large amplitudes between 76° and 78°, and become weak at 71° (Fig. 4(4.4a)). While the ScS amplitudes are comparable to PREM predictions, their arrival times are earlier than predicted. The seismic data can be well explained by a diffusive D″ discontinuity with a shear velocity jump of 3% and transitional depths between 2621 and 2721 km, followed by a negative velocity gradient to 0% at the CMB (Fig. 4(4.4b and c)).

Seismic waves for event 1997/07/11 sample the high-velocity patch in the west. The Scd phases are visible from 68° to 76° (Fig. 4(4.1a)). The amplitudes of Scd phases are large at 68°, which is consistent with the existence of a sharp D″ discontinuity. The seismic data of event 1997/07/11 can be well explained by a sharp discontinuity at 2641 km depth with a shear velocity jump of 5.0%, a negative velocity gradient above the discontinuity from 0% at 2401 km to −1.5% at 2641 km, and a negative velocity gradient below the discontinuity to 0% at the CMB (Fig. 4(4.1b and c)).

4. Relationships between the D″ discontinuity, velocity anomalies in the lowermost mantle, post-perovskite transformation and past subduction

Our differential-travel-time analyses reveal detailed velocity structures in the lowermost 300 km of the mantle beneath Eurasia. There are two high-velocity patches spanning a width of 3000 km and separated by a 300 km-wide normal velocity gap. Maximum shear velocity perturbation reaches 3.8% and compressional velocity perturbation 2.7%. Our waveform modeling indicates that the characteristics of the D″ discontinuity are closely related to the small-scale variations of the velocity anomalies in the lowermost mantle. D″ discontinuities are observed in the high-velocity patches, but not in the normal velocity gap. Though deduced from relatively sparse dataset, our results further indicate that the features of the D″ discontinuity vary in the high-velocity regions, from

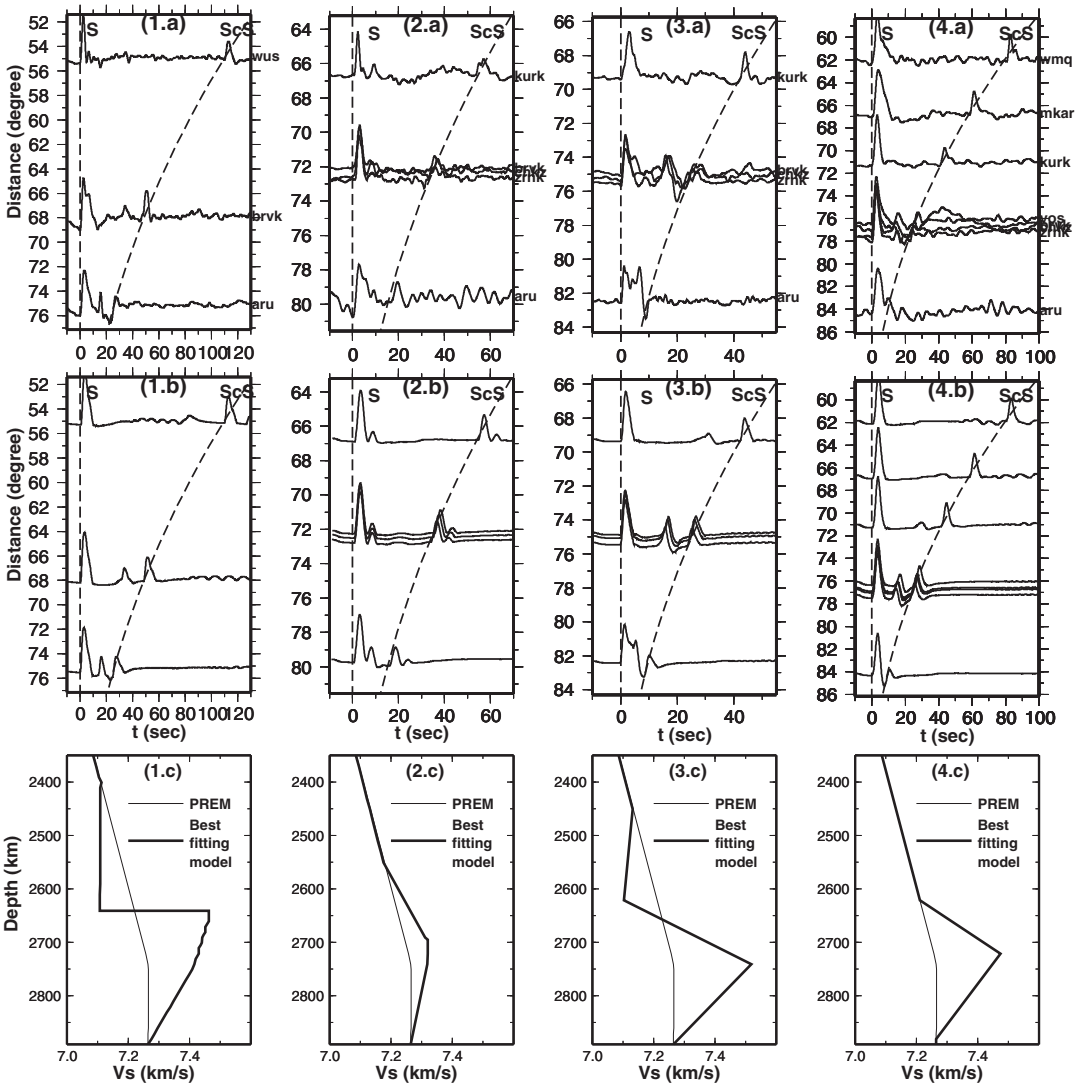

Fig. 4. Top panels: Tangential displacements recorded for four selected events sampling the high velocity area (see Fig. 3 for the sampling region and Table 1 for the events numbered in a same way). Seismic waveforms are aligned along the hand-picked SH arrival times. Middle panels: synthetic seismograms calculated based on one-dimensional (1D) models shown in the bottom panels. The dashed lines are predicted arrivals of S and ScS phases based on PREM. Bottom panels: 1D models (heavy lines) used for calculating synthetics in the middle panels, along with PREM (thin black lines).

a sharp discontinuity in the western patch to a diffusive discontinuity with a transitional depth of at least 100 km in the eastern patch.

Our results of the D″ discontinuity can be explained by the post-perovskite transformation in the lower mantle. The observations that the D″ discontinuities occur only in the high-velocity patches (presumably low temperature regions) are consistent with the positive Clapeyron slope of the post-perovskite transition. The positive Clapeyron slope of the post-perovskite transition implies that the transition should occur at shallower depths in low temperature regions and greater depths in high temperature regions (Murakami et al., 2004). In the present case, the post-perovskite transformation occurs some depths above the CMB in the high-velocity patches because of its low temperature; the transformation would occur at a pressure larger than the CMB pressure in the normal velocity gap because of its relatively high temperature, making the discontinuity disappear there. The observation that the D″ discontinuity disappears in the normal velocity gap can be used to place further constraints on the Clapeyon slope of the post-pervoskite transition, if the temperature difference between the high-velocity regions and the normal velocity gap can be determined.

The varying transitional depths of the D″ discontinuity in the high-velocity region can be explained by compositional effects on the post-perovskite transition in the presence of strong variations of composition within the high-velocity anomalies. It is known that the transitional pressure range of the post-perovskite transition strongly depends on composition. Decreasing Fe^{2+} or Al^{3+} content in perovskite would decrease the post-perovskite transition pressure range, and vice versa (Caracas and Cohen, 2008; Akber-Knutson et al., 2005); an elevated Al content and/or a lower Mg/Si ratio would broaden the post-perovskite transition zone (Catalli et al., 2009). Therefore, the sharp D″ discontinuity inferred in the western high-velocity patch would be consistent with a low aluminum or iron content and/or a high Mg/Si ratio there, while the diffusive D″ discontinuities estimated in the eastern high-velocity patch would indicate the opposite. Unfortunately, this study does not provide accurate estimation of the transitional depths of the diffusive D″ discontinuity in the eastern high-velocity anomalies, due to the lack of seismic observations in the distance range of 68–78°. While a more accurate estimate of the transitional depth of the D″ discontinuity would be expected to place more quantitative constraints on the compositional variations in the region, it would

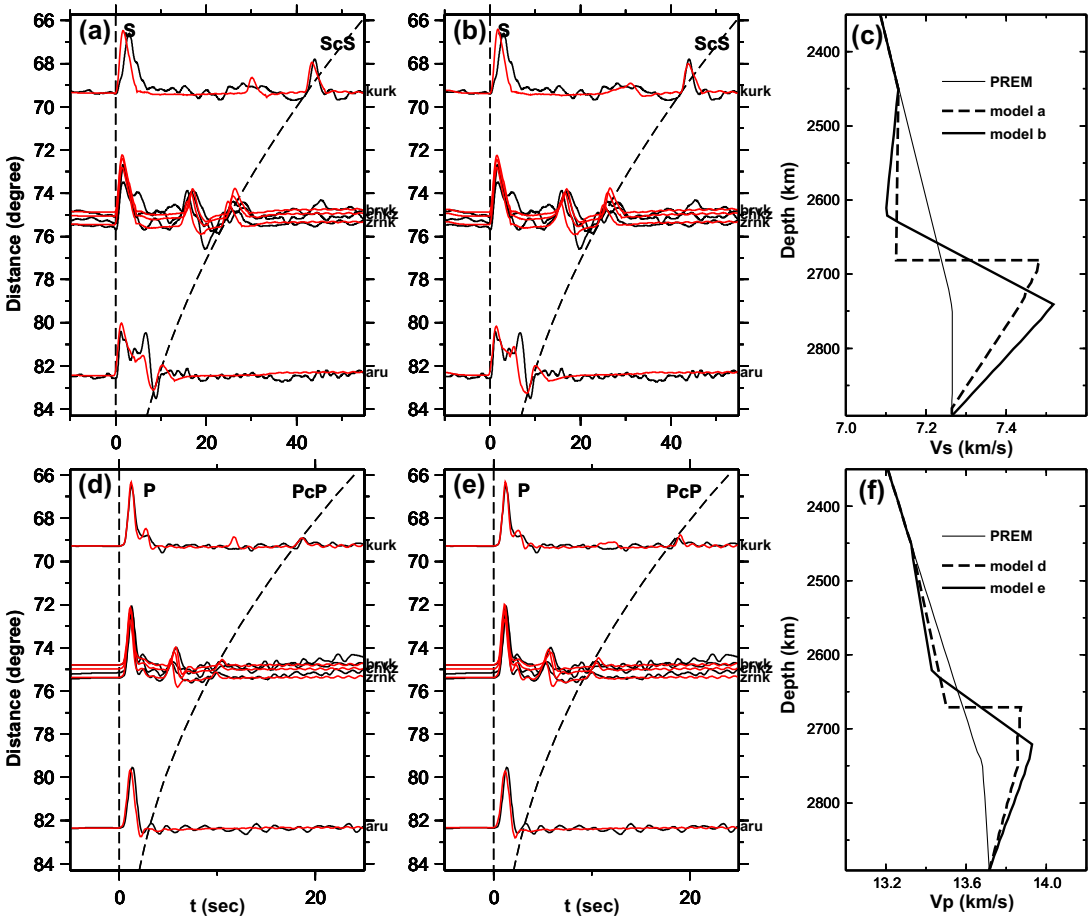

Fig. 5. (a and b) Tangential displacements (black lines) recorded for event 2000/08/07 and synthetics (red lines) calculated based on models with a sharp discontinuity (a) and a discontinuity with a finite depth transition (b) (see models in c). Seismic waveforms are aligned along the hand-picked S arrival times. The predicted ScS arrival times (dashed lines labeled as ScS) are based on PREM. (c) 1D S-wave velocity models used for calculating synthetics in (a) and (b), labeled correspondingly with panels. PREM is also plotted as reference (thin black line). (d) Vertical displacements (black lines) recorded for event 2000/08/07 and synthetics (red lines) calculated based on models with a sharp discontinuity (d) and a discontinuity with a finite depth transition (e) (see models in f). Seismic waveforms are aligned along the hand-picked P arrival times; the predicted PcP arrivals (dashed lines labeled as PcP) are based on PREM; (f) 1D compressional-wave models used for calculating synthetics in (d) and (e), labeled correspondingly with panels. PREM is also plotted as reference (thin black line). (For interpretation of the references to color in this figure legend, the reader is referred to the web version of this article.)

have to wait after new seismic data become available at the distance range of 68–78° in the region.

The geographic correlations of the high-velocity patches with the subduction in the past 30–60 Ma and the normal-velocity gap with the subduction gap raise the possibility that the small-scale high velocity anomalies may be the manifestation of the presence of subduction materials at the CMB. Under this hypothesis, the existence of the D″ discontinuity is intimately related to the presence of the past subduction material at the CMB, and the varying features of the discontinuity further suggest strong variations of composition within the subduction materials at the CMB.

5. Conclusions

By using differential-travel-time residuals of ScSH-SH, sScS-sS, PcP-P and pPcP-pP and forward waveform modeling, we study seismic velocity structures and features of the D″ discontinuity near the CMB beneath eastern Eurasia. The observed ScSH-SH, sScS-sS, PcP-P and pPcP-pP differential-travel-time residuals reveal two high-velocity patches spanning a width of 3000 km and separated by a 300-km wide normal-velocity gap. The maximum shear and compressional velocity perturbations in the lowermost 300 km of the mantle reach 3.8% and 2.7%, respectively. Detailed waveform modeling shows that the D″ discontinuity emerges in the high velocity patches and disappears in the normal velocity gap. Furthermore, the features of the D″ discontinuity vary from diffuse D″ discontinuities in the eastern patch to sharp D″ discontinuities in the western patch. The diffuse D″ discontinuities in the eastern patch start at 270 km above the CMB and have shear velocity jumps of 3.0–5.0% and depth transitions of at least 100 km, while the sharp D″ discontinuities in the western patch occur at 250 km above the CMB and have shear velocity jumps of 5.0%. A diffusive P wave discontinuity is also detected in the eastern patch and has similar features as those of the S wave discontinuity. The inferred features of the D″ discontinuity, including its presence/absence and varying characteristics from a sharp discontinuity to a diffusive one, can be explained by the post-perovskite transition in the lower mantle with variations of temperature and composition. The high-velocity patches and the presence of the D″ discontinuity geographically correlate with the reconstructed locations of ancient Indian and Pacific subducted slabs, while the normal-velocity gap and the absence of the D″ discontinuity there fall into the past subduction gap. These geographical correlations raise the possibility that the presence of the D″ discontinuity may be related to ancient subducted materials at the CMB, and the varying features of the D″ discontinuity further suggest existence of strong compositional variations within the subduction materials at the CMB.

Acknowledgments

We gratefully acknowledge the participants of the Data Management Center of China National Seismic Network at Institute of Geophysics, China Earthquake Administration, the F-net and the Incorporated Research Institutions for Seismology for their efforts in collecting the data. We thank Satoru Tanaka and Keke Zhang for their reviews and comments that improved the paper significantly. We also thank Yi Wang for providing the code for upper mantle anisotropy correction of station ARU. Figures were made with the General Mapping Tools (Wessel and Smith, 1995). This work was supported by the National Science Foundation of China (40774041 and 41074059) and an NSF grant #0911319.

References

Akber-Knutson, S., Steinle-Neumann, G., Asimow, P.D., 2005. Effect of Al on the sharpness of the $MgSiO_3$ perovskite to post-perovskite phase transition. Geophys. Res. Lett. 32, L14303. doi:10.1029/2005GL023192.

Caracas, R., Cohen, R.E., 2008. Ferrous iron in post-perovskite from first-principles calculations. Phys. Earth Planet. In. 168, 147–152.

Catalli, K., Shim, S., Prakapenka, V., 2009. Thickness and clapeyron slope of the post-perovskite boundary. Nature 462. doi:10.1038/nature08598.

Chaloner, J.W., Thomas, C., Rietbrock, A., 2009. P- and S-wave reflectors in D″ beneath southeast Asia. Geophys. J. Int. 179, 1080–1092. doi:10.1111/j.1365-246X.2009.04328.

Dziewonski, A.M., Anderson, D.L., 1981. Preliminary reference Earth model. Phys. Earth Planet. In. 25, 297–356. doi:10.1016/0031-9201(81)90046-7.

Ding, X., Helmberger, D.V., 1997. Modelling D″ structure beneath Central America with broadband seismic data. Phys. Earth Planet. In. 101, 245–270.

Grand, S.P., 2002. Mantle shear-wave tomography and the fate of subducted slabs. Philos. Trans. R. Soc. A 360, 2475–2491.

Gu, Y.J., Dziewonski, A.M., 1999. Mantle discontinuities and 3-D tomographic models. EOS Trans. AGU 80, F717.

He, Y., Wen, L., Zheng, T., 2006. Geographic boundary and shear wave velocity structure of the ''Pacific anomaly'' near the core-mantle boundary beneath western Pacific. Earth Planet. Sci. Lett. 244, 302–314.

Hirose, K., 2006. Postperovskite phase transition and its geophysical implications. Rev. Geophys. 44, RG3001. doi:10.1029/2005RG000186.

Hutko, A.R., Lay, T., Revenaugh, J., Garnero, E.J., 2008. Anticorrelated seismic velocity anomalies from post-perovskite in the lowermost mantle. Science 320, 1070–1074.

Kito, T., Rost, S., Thomas, C., Garnero, E.J., 2007. New insights into the P- and S-wave velocity structure of the D″ discontinuity beneath the Cocos plate. Geophys. J. Int. 169, 631–645.

Lay, L., Helmberger, D.V., 1983. A lower mantle S-wave triplication and the shear velocity structure of D″. Geophys. J. Roy. Astr. S. 75, 799–837.

Lay, T., Garnero, E.J., Williams, Q., 2004. Partial melting in a thermo-chemical boundary layer at the base of the mantle. Phys. Earth Planet. In. 146, 441–467.

Lay, T., 2008. Sharpness of the D″ discontinuity beneath the Cocos plate: implications for the perovskite to post-perovskite phase transition. Geophys. Res. Lett. 35, L03304. doi:10.1029/2007GL032465.

Li, C., van der Hilst, R.D., Engdahl, E.R., Burdick, S., 2008. A new gloabl model for P wave speed variations in Earth's mantle. Geochem. Geophys. Geosyst. 9, Q05018. doi:10.1029/2007GC001806.

Masters, G., Laske, G., Bolton, H., Dziewonski, A., 2000. The relative behavior of shear velocity, bulk sound speed, and compressional velocity in the mantle: implications for chemical and thermal structure. In: Karato, S., Forte, A.M., Liebermann, R.C., Masters, G., Stixrude, L. (Eds.), Earth's Deep Interior, AGU Monograph 117. AGU, Washington, DC.

Mégnin, C., Romanowicz, B., 2000. The three-dimensional shear velocity structure of the mantle from the inversion of body, surface and higher-mode waveforms. Geophys. J. Int. 143, 709–728.

Murakami, M., Hirose, K., Kawamura, K., Sata, N., Ohishi, Y., 2004. Post-perovskite phase transition in $MgSiO_3$. Science 304, 855–858.

Obayashi, M., Sugioka, H., Yoshimitsu, J., Fukao, Y., 2006. High temperature anomalies oceanward of subducting slabs at the 410-km discontinuity. Earth Planet. Sci. Lett. 243, 149–158.

Oganov, A.R., Ono, S., 2004. Theoretical and experimental evidence for a post-perovskite phase of $MgSiO_3$ in Earth's D″ layer. Nature 430, 445–448.

Ritsema, J., van Heijst, H.-J., 2000. Seismic imaging of structural heterogeneity in Earth's mantle: evidence for large-scale mantle flow. Sci. Prog. 83, 243–259.

Ritsema, J., Deuss, A., van Heijst, H.J., Woodhouse, J.H., 2010. S40RTS: a degree-40 shear-velocity model for the mantle from new Rayleigh wave dispersion, teleseiesmic traveltime and normal-mode splitting function measurements. Geophys. J. Int.. doi:10.1111/j.1365246X.2010.04884.

Shim, S., 2008. The postperovskite transition. Annu. Rev. Earth Planet. Sci. 36, 569–599.

Silver, P.G., 1996. Seismic anisotropy beneath the continents: probing the depths of geology. Annu. Rev. Earth Plane. Sci. 24, 385–432.

Thomas, C., Kendall, J.-M., Weber, M., 2002. The lowermost mantle beneath northern Asia-I. Multi-azimuth studies of a D″ heterogeneity. Geophys. J. Int. 151, 279–295.

Thomas, C., Kendall, J.-M., Lowman, J., 2004. Lower-mantle seismic discontinuities and the thermal morphology of subducted slabs. Earth Planet. Sci. Lett. 225, 105–113.

Van der Hilst, R.D., Kárason, H., 1999. Compositional heterogeneity in the bottom 1000 km of Earth's mantle: towards a hybrid convection model. Science 283, 1885–1888.

Weber, M., Davis, J.P., 1990. Evidence of a laterally variable lower mantle structure from P- and S-waves. Geophys. J. Int. 102, 231–255.

Weber, M., 1993. P- and S-wave reflection from anomalies in the lowermost mantle. Geophys. J. Int. 115, 183–210.

Wen, L., 2002. An SH hybrid method and shear velocity structures in the lowermost mantle beneath the central Pacific and South Atlantic Oceans. J. Geophys. Res. 107. doi:10.1029/2001JB000499.

Wen, L., Anderson, D.L., 1995. The fate of slabs inferred from seismic tomography and 130 million years of subduction. Earth Planet. Sci. Lett. 133, 185–198.

Wessel, P., Smith, W.H.F., 1995. New version of the generic mapping tools released EOS. EOS T. Am. Geophys. Un. 76, 329.

Wookey, J., Stackhouse, S., Kendall, J.-M., Broadholt, J., Price, G.D., 2005. Efficacy of the post-perovskite phase as an explanation for lowermost-mantle seismic properties. Nature 438, 1004–1007.

Wysession, M., Lay, T., Revenaugh, J., Williams, Q., Garnero, E.J., Jeanloz, R., Kellogg, L., 1998. The D″ discontinuity and its implications. In: Gurnis, M., Wysession, M.E., Knittle, E., Buffett, B.A. (Eds.), The Core-Mantle Boundary Region. AGU, Washington, DC, pp. 273–298.

Young, G.J., Lay, T., 1990. Multiple phase analysis of the shear velocity structure in the D'' region beneath Alaska. J. Geophys. Res. 95, 17385–17402.

Zhao, D., 2004. Global tomographic images of mantle plumes and subducting slabs: insight into deep Earth dynamics. Phys. Earth Planet. In. 146, 3–34.